# Effects of gate-induced electric fields on semiconductor Majorana nanowires

Andrey E. Antipov,[1,*] Arno Bargerbos,[2,3] Georg W. Winkler,[1] Bela Bauer,[1] Enrico Rossi,[4,1] and Roman M. Lutchyn[1]

[1] *Station Q, Microsoft Research, Santa Barbara, California 93106-6105, USA*
[2] *QuTech, Delft University of Technology, 2600 GA Delft, The Netherlands*
[3] *Kavli Institute of Nanoscience, Delft University of Technology, 2600 GA Delft, The Netherlands*
[4] *Department of Physics, William & Mary, Williamsburg, VA 23187, USA*

(Dated: January 9, 2018)

We study the effect of gate-induced electric fields on the properties of semiconductor-superconductor hybrid nanowires which represent a promising platform for realizing topological superconductivity and Majorana zero modes. Using a self-consistent Schrödinger-Poisson approach that describes the semiconductor and the superconductor on equal footing, we are able to access the strong tunneling regime and identify the impact of an applied gate voltage on the coupling between semiconductor and superconductor. We discuss how physical parameters such as the induced superconducting gap and Landé g-factor in the semiconductor are modified by redistributing the density of states across the interface upon application of an external gate voltage. Finally, we map out the topological phase diagram as a function of magnetic field and gate voltage for InAs/Al nanowires.



## I. INTRODUCTION

Composite heterostructures provide an opportunity to realize exotic phases of matter by exploiting the properties of individual components. A particularly interesting example involves semiconductor-superconductor hybrid structures which represent a promising platform for the realization of topological superconductivity [1–9]. Topological superconductors support exotic neutral excitations consisting of an equal superposition of an electron and a hole – Majorana zero-energy modes (MZMs) [10–12]. Due to the particle-hole symmetry in a superconductor, such modes appear at zero energy and, thus, there is no cost to occupy these states. This leads to a growing degeneracy of the ground state as the number of MZMs is increased, a hallmark of topological superconductors. Theory predicts that exchanging the position of MZMs [10, 13] or performing certain non-local measurements of the charge encoded in a collection of MZMs [14] leads to a nontrivial transformation within the degenerate ground-state manifold, and represents a non-Abelian operation which is independent of the details of its execution. This property of topological superconductors has generated a lot of excitement in the condensed matter physics, quantum information, and material science communities [15–18] as it opens up the possibility of Majorana-based topological quantum computing [6, 9, 19, 20].

Realizing topological superconductivity in the laboratory is not an easy task since the originally proposed models [10, 12] involved spinless p-wave superconductivity. Electrons in solids have spin-$\frac{1}{2}$ and most of the common superconductors have s-wave pairing which involves electrons with opposite spins. Therefore, quenching spin degeneracy and preserving superconducting pairing is quite non-trivial. One way to overcome the problem is to use materials with a strong spin-orbit interaction which couples spin and orbital degrees of freedom. A number of platforms for realizing MZMs in the laboratory have been recently proposed [21–48]. The most promising proposal for realizing MZMs is based on one-dimensional (1D) semiconductor-superconductor (SM-SC) hybrid structures [27, 28] and involves a semiconductor with strong spin-orbit coupling (such as InAs or InSb) and an s-wave superconductor (such as Al). In this proposal, a magnetic field or another time-reversal breaking perturbation is needed to drive the system into the spinless topological regime [27, 28]. This proposal has triggered significant experimental activity [49–69], and there is a compelling body of experimental evidence that MZMs have been realized in these systems. For a very recent example, see Ref. [64] which reports a robust quantized $2e^2/h$ zero-bias conductance consistent with the Majorana scenario.

Much of the progress in realizing MZMs with proximitized nanowires is attributed to the material science advance in fabricating semiconductor-superconductor heterostructures. In the first generation of experiments [49–54] the superconductor was deposited ex-situ which required removing the native oxide forming on the semiconductor's surface due to air exposure. In the second generation of experiments the thin aluminum shell [70] is deposited epitaxially and is thus grown on pristine SM facets without breaking the vacuum, see Fig. 1. Tunneling spectroscopy measurements of the induced superconducting gap [55, 60, 62, 64, 68] in such samples exhibit a large induced gap (i.e. close to the bulk gap of the superconductor) which indicates that the improved epitaxial interfaces are characterized by a strong hybridization of the states in the semiconductor and superconductor. In this strong tunneling regime, many physical parameters such as the g-factor and spin-orbit coupling are strongly renormalized due to the hybridization. In order to quantitatively understand the hybridization and its implications on the band structure as well as other physical properties, one has to consider the band offset

* andrey.antipov@microsoft.com

at the superconductor-semiconductor interface. Depending on the sign of the band offset one can have either a Schottky barrier or an accumulation layer [71–74]. Based on preliminary ARPES studies [75], one finds that the band offset for epitaxially grown InAs/Al heterostructures is $-(200-300)$meV supporting the accumulation layer scenario.

Proper theoretical treatment of the strong coupling regime is also necessary to understand how external gates affect the electronic state, and in particular the topological nature, of SM-SC heterostructures. Furthermore, recent proposals for realizing scalable architectures for topological quantum computation with MZMs rely on fine electrostatic control [76–80]. Thus, understanding the effect of electric fields on the low-energy properties of the proximitized nanowires is critical both for the interpretation of the existing Majorana experiments [57, 60, 62, 64, 68] as well as for the optimization of proposed Majorana devices [9].

In order to understand the physical properties of the proximitized nanowires, one needs to solve the electrostatic and quantum-mechanical problems self-consistently, i.e. perform Schrödinger-Poisson (SP) calculations. Compared to the case of purely semiconducting heterostructures [81–83], the problem at hand is much more challenging technically because it involves disparate materials with very different effective masses, Fermi energies, $g$-factors etc. (see Table I). In other words, the standard numerical tools based on the continuum mass approximation cannot be applied to semiconductor-superconductor hydrid systems. Therefore, modeling of the semiconductor-superconductor hybrid structures requires developing numerical techniques which can effectively take into account different length scales in the semiconductor and superconductor.

Previous effective models for superconductor-semiconductor hybrids [84–89] do not properly describe the experimental system and provide only qualitative predictions for the electric field dependence. These models rely on independent phenomenological parameters such effective masses, spin-orbit couplings, g-factors as well as tunneling strength between semiconductor and superconductor. While this approach may be suitable for the weak tunneling regime, naive extensions of such models to the strong coupling limit are inadequate. This is because the electric field applied to the semiconductor can drastically change the electrons' confinement, i.e. push or pull electron density in the semiconductor to or away from the interface. This in turn strongly affects physical parameters of the system, including, as we will see, the tunneling rate, effective spin-orbit coupling, $g$-factor as well as induced superconducting gap.

More advanced models have been introduced recently [90–93] which treat the effects of an electric field within some effective models where the superconductor is taken into account via boundary conditions. This approach, while being computationally advantageous, does not take into account the effects arising from the redistribution of the wavefunction between the semiconductor and the superconductor. In this work, we treat the superconducting (SC) and semiconducting (SM) degrees of freedom explicitly on the same footing. Using an adaptive discretization algorithm for the SM and SC components, we develop an effective model which is computationally tractable and allows us to adequately capture the effect of the gate-induced electric field on the heterostructure. Our results allow one to understand and interpret recent experiments investigating electric field dependence of the effective parameters [57, 60, 62, 64, 68].

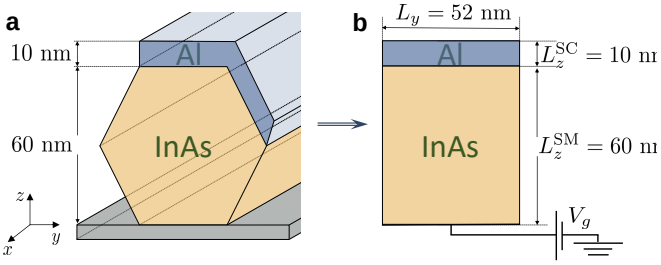


FIG. 1. (a) SM-SC heterostructure based on hexagonal nanowire. 10 nm thick Al layer (blue) is deposited on 2 facets of InAs (brown) hexagonal wire with a height of 60 nm. The back gate is shown schematically in gray. (b) Rectangular geometry of the wire that supports the same number of subbands. The back gate is emulated by a boundary condition at the bottom.

The paper is organized as follows. We begin with a discussion of the Setup and Methods in Sec. II where we provide technical details of the Schrödinger-Poisson approach. In Sec. III we present our results. We first focus on the limit of zero magnetic field and then discuss the behavior at finite magnetic fields. We conclude the section with the discussion of the topological phase diagram. We summarize our results in Sec. IV and discuss their relevance for current and future experiments.

## II. SETUP AND METHODS

We consider the system shown in Fig. 1. The nanowires used in current experiments typically have a hexagonal shape as shown in Fig. 1 (a). The cross section of the wire, which we take to be the $(y,z)$-plane, consists of a 10 nm thick Al film (blue) covering 2 facets of InAs nanowire (orange). The electrostatic environment is controlled by a back-gate (gray). For practical reasons we do not explicitly treat this gate and the separating dielectric medium in our calculations, but rather take the gate into account only as a boundary condition for the potential in the wire. In order to convert this into the actual voltage applied to the gate (which is sample-dependent), the distance to the gate and the dielectric constant have to be taken into account. For the devices of interest, the length of the wire, $L_x$, is much larger than its transverse dimensions $L_{y,z}$.

| Parameter | InAs | Al |
|---|---|---|
| $m^*$ | 0.026 [94] | 1 |
| $\epsilon_r$ | 15.15 | |
| $W$, eV | $-0.25$ | |
| $g^{\rm bare}$ | $-15$ [95] | 2 |
| $\alpha$, eV$\cdot$ nm | 0.01 [96] | 0 |
| $\varepsilon_F$, eV | 0 | 11.27 [97] |
| $\Delta_0$, meV | 0 | 0.34 [97] |
| $L_z$, nm | 60 | 10 |
| $L_y$, nm | 52 | 52 |

TABLE I. Physical parameters for InAs and Al.

The presence of the Al layer breaks the hexagonal symmetry of the nanowire cross section and, as shown in Fig. 2, causes the formation of an electrostatic potential that strongly confines the electrons close to the SM/Al interface. For this reason the hexagonal cross section of the wire can be well approximated by an effective rectangular cross section, as shown in Fig. 1 (b). We will henceforth refer to the effective wire with rectangular cross section as the *slab model*. By choosing $L_y$ for the slab model to be such that the number of cross sectional modes is the same as for the hexagonal cross section wire, the use of the slab model does not cause any significant loss of accuracy and significantly simplifies the numerical implementation and solution of the SP problem.

The Hamiltonian for the heterostructure in the normal state can be written as ($\hbar = 1$)

$$\hat{H}_n = -\partial_z \left[\frac{1}{2m^*(z)}\partial_z\right] + \frac{1}{2m^*(z)}\left(\hat{k}_x^2 + \hat{k}_y^2\right) \tag{1}$$
$$+\phi(z) - \varepsilon_F(z) - \alpha(z)\left(\hat{k}_x\hat{\sigma}_y - \hat{k}_y\hat{\sigma}_x\right) + \frac{\mu_B g^{\rm bare}(z) B}{2}\hat{\sigma}_x,$$

where the spatially-dependent effective mass $m^*(z)$, Fermi energy $\varepsilon_F(z)$, spin-orbit coupling strength $\alpha(z)$, and $g$ factor $g(z)$ are equal to $m^*(z) = m_{SM}$ ($m^*(z) = m_{SC}$) for $z < 60$ nm ($z > 60$ nm) and similarly for $\varepsilon_F(z)$, $\alpha(z)$, and $g(z)$; $\hat{k}_x, \hat{k}_y$ are the momentum operators in the $x$ and $y$ direction, respectively; $\phi(z)$ is the electrostatic potential, $\sigma_{x,y,z}$ are the Pauli-matrices in spin space, $\mu_B$ and $B$ are the Bohr magneton and the external magnetic field, respectively. The values for the material parameters used henceforth are given in Table I.

In this work we investigate bulk properties of the heterostructure. Therefore, we assume henceforth that the nanowire is infinitely long and translationally invariant along the $x$ direction. This allows one to use as a basis plane waves along the $x$ direction and to replace the operator $\hat{k}_x$ in (1) by its eigenvalue. In the clean limit considered here, due to the finite-size quantization in the $y$ and $z$ directions, the spectrum of the system consists of effectively 1D subbands. We obtain the eigenvalues and eigenstates of the resulting Hamiltonian $\hat{H}_n(\hat{k}_x \to k_x)$ corresponding to these subbands via a mode decomposition in the $y$ direction and by replacing the derivatives with respect to $z$ with finite differences using a non-uniform grid [98] with two different spacings corresponding to the semiconducting and superconducting components, respectively. The spacings are chosen such that $dz < \pi/k_F$ in order to minimize discretization errors. Using a non-uniform spacing significantly alleviates the computational cost and allows us to systematically study the phase diagram of the problem.

In the absence of spin-orbit coupling the discrete modes along the $y$ direction are

$$\psi_{n_y}^{\alpha=0}(y) = \sqrt{\frac{2}{L_y}}\sin\left(\frac{\pi n_y}{L_y}y\right) \tag{2}$$

with the different $n_y \in \mathbb{N}$ modes being decoupled. The spin-orbit coupling term hybridizes them [84]. The corresponding matrix elements are

$$\begin{aligned}\mathcal{A}_{n_y n_y'}(z) =& \alpha(z)\langle\Psi_{n_y}^{\alpha=0}|\frac{d}{dy}|\Psi_{n_y'}^{\alpha=0}\rangle \\ =& \frac{2\alpha(z)}{L_y}(-1+(-1)^{n_y+n_y'})\frac{n_y n_y'}{n_y^2-(n_y')^2}.\end{aligned} \tag{3}$$

In the $\{\psi_{k_x,n_y,z} = e^{ik_x x}\Psi_{n_y}^{\alpha=0}(y)\delta(z)\}$ basis the Hamiltonian matrix takes the form

$$\tilde{H}_n = \langle\psi_{k_x,n_y,z}|\hat{H}_n^{\alpha=0}|\psi_{k_x,n_y,z}\rangle + \mathcal{A}_{n_y n_y'}(z)\otimes\sigma_x. \tag{4}$$

We treat the s-wave superconductor at the BCS mean-field level. The Bogoliubov-de-Gennes (BdG) Hamiltonian for the system can be written as

$$H = \tilde{H}_n \otimes \hat{\tau}_z - \Delta(z)\hat{\sigma}_y \otimes \hat{\tau}_y, \tag{5}$$

where $\hat{\tau}_z$, $\hat{\tau}_y$ are Pauli matrices in Nambu (particle-hole) space. We include the superconducting pairing only in the superconductor, i.e. $\Delta(z) = \Delta_0$ for $z > 60$ nm, where $\Delta_0$ is the SC gap of Al (see Table I), and $\Delta(z) = 0$ for $z < 60$nm. In a finite magnetic field, the superconducting gap in the Al shell is suppressed due to the inclusion of a finite $g$-factor for the Al (see Table I). Given that the Al film is very thin, see Fig. 1, we neglect orbital effects due to the magnetic field.

### A. Electrostatics

In order to obtain the electrostatic profile, one has to solve the SP equations self-consistently. Given that the BCS mean-field approximation breaks charge conservation this is a non-trivial task, see, e.g., discussion in Ref. [99]. However, electrostatic screening of a metal is only weakly modified by the superconductivity with the small parameter being $\Delta_0/\epsilon_F \ll 1$. As a consequence, to obtain the electrostatic potential within this accuracy the charge density entering the Poisson equation can be calculated neglecting the superconducting pairing, i.e. using the Hamiltonian $H_n(k_x)$ instead of the full Hamiltonian

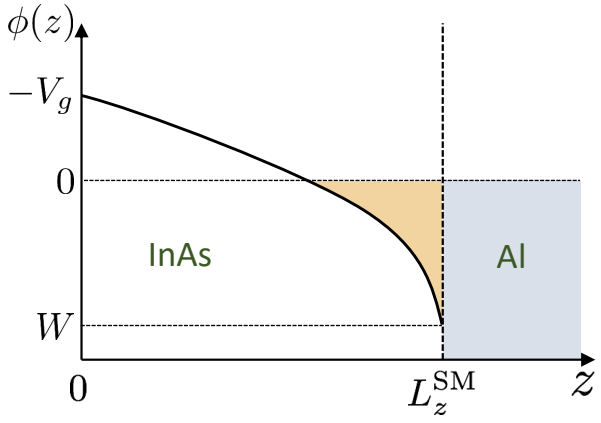


FIG. 2. The electrostatic calculation uses Dirichlet boundary conditions at $z = 0$ and $z = L_z^{\mathrm{SM}}$, i.e. the top and bottom of the semiconducting wire. At $z = 0$, the boundary condition is given by the gate voltage $V_g$, while at the interface to the aluminum it is given by the band offset $W$ (see also Table I). This leads to an accumulation layer at the interface.

$H$. The effects of the spin-orbit coupling and Zeeman terms [91] on the total electron density profile $n(z)$ are also very small and can be neglected. Thus, to solve the full problem we follow a two step approach: we first solve the SP problem in the normal state taking $\alpha = 0$ and $B = 0$ to obtain the electrostatic profile. We then use the obtained electrostatic profile to find the eigenvalues and the eigenstates of the system for $\Delta_0 \neq 0$, $\alpha \neq 0$, and different values of $B$.

The first step consists in solving self-consistently the Schrödinger equation $H_n|\Psi\rangle = E|\Psi\rangle$, requiring $\Psi$ to vanish at the boundaries of the system, [100] and the Poisson equation

$$\partial_z^2 \phi(z) = -\frac{n(z)}{\epsilon_0 \epsilon_r}, \tag{6}$$

where $n(z) = (2\pi L_y)^{-1} \sum_{n_y, E[\Psi]<=0} \int dk_x \left|\Psi_{k_x,n_y}(z)\right|^2$, $\epsilon_r$ is the relative dielectric constant of the SM, see Tab. I, and $\epsilon_0$ is the vacuum dielectric constant. The setup for the Poisson equation is shown in Fig. 2. At $z = L_z^{\mathrm{SM}}$ the boundary condition for $\phi(z)$ is given by the band offset $W$ between the SM and the SC. The boundary condition at $z = 0$ is set by the back gate. The coupled Schrödinger-Poisson equations are solved iteratively until convergence is achieved, using Anderson's mixing algorithm [101].

### B. Band structure

The calculated electrostatic profile $\phi(z)$ is inserted into the full Hamiltonian $H$ to obtain the band structure $\{\varepsilon^{(n)}(k_x)\}$ and the corresponding eigenstates of the nanowire. Since the chemical potential is included in the Hamiltonian, the effective Fermi energy for each band is set simply by the bottom of the band. We can find the Fermi momentum in each band, $k_F^{(n)}$, by solving $\varepsilon^{(n)}(k_F^{(n)}) = 0$. The Fermi velocity is given by $v_F^n = \frac{d\varepsilon^{(n)}}{dk^{(n)}}|_{k^{(n)}=k_F^{(n)}}$. In addition, from the eigenstates at $k = k_F$ we extract how strongly different subbands are coupled to the superconductor, which we define through the weight of the corresponding state in the superconductor

$$W_{\mathrm{SC}} = 1 - \sum_{n_y,\sigma} \int_0^{L_z^{\mathrm{SM}}} |\Psi(k_F)|^2 dz \tag{7}$$

We define the gap as the minimum of the energy of the first excited state: $E_g = \min_{k_x} |\varepsilon^{(n)}_{\mathrm{BDG}}(k_x)|$. At zero magnetic field, $E_g$ gives an estimate for the induced gap $\Delta = E_g(B = 0)$.

## III. RESULTS

In this section we discuss the results of our numerical simulations. We first discuss only the electrostatic problem for both a model of a hexagonal wire and the slab model introduced above. We then investigate the nature of the electronic states in a limit of strong coupling between the semiconductor and superconductor and discuss their superconducting properties at zero magnetic field. Then we study properties of the hybrid nanowires in a finite magnetic field and obtain estimates for the effective g-factor in the hybrid structure. Finally, we present the topological phase diagram and compare it with previous results [84, 102].

### A. Electrostatics and density distribution

#### 1. *Hexagonal cross section*

In order to obtain the correct number of subbands for a given gate configuration for the wire with the hexagonal cross section it is sufficient to solve the SP problem using the Thomas Fermi approximation and simply requiring the wave function to vanish at the boundaries of the cross section. The solution of the full SP problem is computationally expensive due to the shape of the cross section and unnecessary for the purpose of simply estimating the number of cross sectional modes. We perform this calculation in COMSOL and obtain eigenstates using the Kwant package [103].

Our results are summarized in Fig. 3, where we show the density for all occupied modes below the Fermi energy. This calculation does not explicitly treat the aluminum shell; instead, it assumes that the only effect of the presence of the Al layer is to induce a band offset. We set this band offset to $W = -0.25$ eV [75], see Table I. The approximations used to obtain the results of Fig 3 cause quantitative inaccuracies for the local density

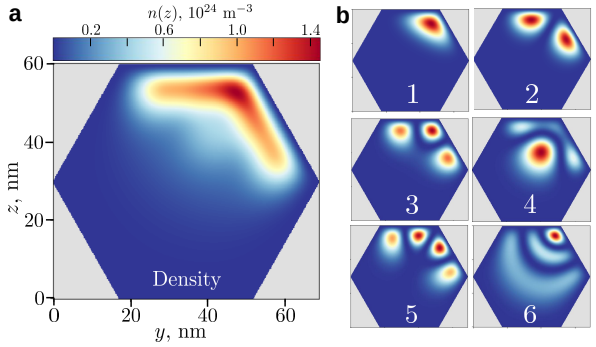


FIG. 3. (a) Electronic density in the cross-sectional cut of the nanowire for $V_g = 0$ obtained the Thomas Fermi approximation. (b) Square modulus of eigenstates of the wire in the normal state at $B = 0$ with energies $-0.096$, $-0.068$, $-0.052$, $-0.023$, $-0.021$, and $-0.006$ eV for panels 1 to 6 respectively.

of states (LDOS) and the carrier density profile. However, these results are sufficiently accurate to estimate the number of electronic cross-sectional modes below the Fermi energy for a given $V_g$. In addition, the results of Fig. 3 (a) show the qualitatively correct result that for $V_g \leq 0$ most of the charge density is localized at the semiconductor (SM)-superconductor (SC) interface due to the strong band offset between the InAs and Al. This fact means that for the slab model, the thickness of the SM wire in the $z$ direction does not affect the electronic properties in a significant way as long as it is few times larger than the confinement length in the $z$ direction ($\sim 20$ nm). The effective width $L_y$ of the slab model can then be fixed by requiring the number of subbands to be equal to the number of cross-sectional modes obtained from the hexagonal calculation, as long as $L_y$ is also larger than the confinement length in the $z$ direction. For $V_g = 0$ the hexagonal cross section results show that there are six modes, see Fig. 3 (b). From this we obtain that for the slab model $L_y = 52$ nm, larger than the confinement length for $V_g = 0$. In the remainder all the results are obtained using the effective slab model with $L_y = 52$ nm width and $L_z^{\rm SM} = 60$ nm thickness for the SM and $L_z^{\rm (SC)} = 10$ nm for Al, as shown in Table I.

### 2. *Slab model*

We now switch to the slab model, which explicitly treats the superconducting Al shell. We self-consistently solve the coupled Schrödinger-Poisson (SP) equations for three different values of $V_g$ to obtain the electrostatic potential $\phi(z)$ and the density $n(z)$, respectively shown in panels (a) and (b) of Fig. 4. Since the Al shell is taken to be metallic with an extremely short screening length, the electrostatic potential is assumed to be constant throughout the Al. The dashed line in Fig. 4 (a) shows the Fermi level in Al. It is worth pointing out that because $\Delta_0 \ll \epsilon_F$, including the pairing term for the Al makes only a negligible difference to the electrostatic profile.

For $V_g \leq 0$ the electrostatic potential confines the carrier density in a layer about 20 nm wide close to the SM/Al interface, as shown in Fig. 4 (b). For $V_g > 0$ the electrostatic potential is below the Fermi energy also on the gate side. This allows the accumulation of charges also near the gate, as shown by the result in Fig. 4 (b) for $V_g = 0.2$ $V$.

## B. Nature of electronic states in strong-coupling limit

We now discuss the nature of the electronic states in the electrostatic environment determined by the gate as well as the band offset between the semiconducting wire and the metallic shell. In particular, we will investigate how strongly states are hybridized between the two materials depending on the gate voltage.

In the top panels of Fig. 5, we show the electrostatic profile (cf. Fig. 4) for three values of the gate voltage. The lower panels show the square of the wave function $|\Psi_{k_x=0,n_y}(z)|^2$ for all occupied subbands for the corresponding electrostatic profile. Here we have chosen the momentum of the band bottom, $k_x = 0$, so that all filled bands are included. The color scale in Fig. 5 indicates the weight of the wavefunctions in the superconductor (see Eqn. (7)). In the top panels, we have also superimposed horizontal lines showing the energy of the corresponding subbands; furthermore, the intensity of the lines shows the square magnitude of the wave functions, and in the semiconducting part the color scale indicates again the weight in the superconductor.

For the case of $V_g = 0$ (middle column of panels), we find 9 hybridized subbands, some of which are mostly localized in the SM whereas the others have large weight in the superconductor [104].

For $V_g < 0$ the electrostatic potential confines the wave function in the SM to a very narrow region close to the SM/Al interface. Such confinement favors a strong hybridization of the SM and Al eigenstates, thus giving rise

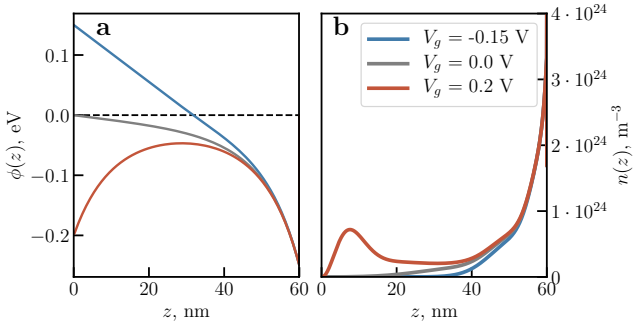


FIG. 4. (a) Electrostatic potential profile $\phi(z)$ and (b) electronic density $n(z)$ in the semiconducting part of the system obtained from a self-consistent Schrödinger-Poisson calculation for three representative values of the gate voltage.

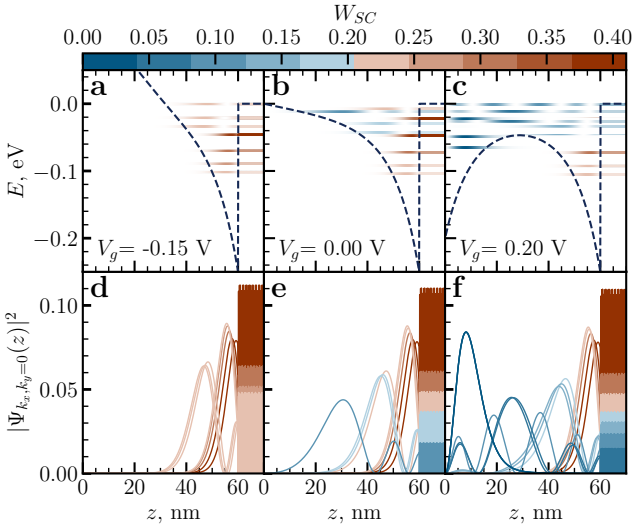


FIG. 5. Eigenstates of the Hamiltonian (4) at $k_x = 0$ for $V_g = -0.15$V, $V_g = 0$V, and $V_g = 0.2$V. The top panel shows the electrostatic potential for reference purposes, with horizontal lines denoting the bottom of each band below the Fermi energy. The color scale indicates the weight in the superconductor, and in the semiconducting part, the intensity indicates the square modulus of the eigenstate. The lower panel shows the eigenfunctions explicitly with the same color coding.

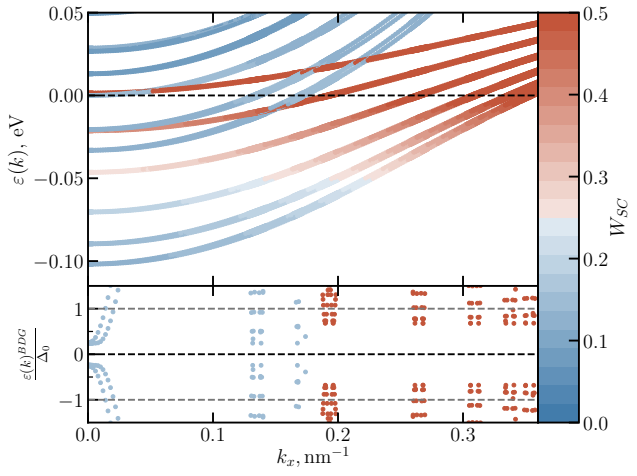


FIG. 6. Top: band structure in the normal state at $V_g = -0.15$ V. Color indicates the weight of the state in the superconductor. Hybridization between states is seen by the changing color of the subbands. Bottom: band structure of the system in the superconducting state. The induced gap in each subband depends on the hybridization to the superconductor. It can clearly be seen that bands with stronger hybridization (red colors) are characterized by a larger induced gap. Here we used the same parameters as in Fig. 5(a) and (d).

to states which have large weight in both the SM and Al. Such large hybridization is prevented in the absence of the confining electrostatic potential due to the large mismatch between the Fermi velocities of the two materials. The strong confining potential due to the band offset is therefore critical for the hybridization of the SM and Al states.

For $V_g > 0$, we see in Fig. 5 (c) that a number of subbands closer to the Fermi energy appear which are not confined to the interface, and instead have appreciable weight throughout the SM. These states have very small $W_{sc}$. Their contribution to the density can also be seen in panel (b) of Fig. 4 in the peak of the density near the gate.

While one might naively expect that the lowest bands are most confined to the interface and thus hybridize most strongly, this is not reflected in the data shown in Fig. 5. To further elucidate which bands most strongly hybridize with the superconductor, we show the full band structure at $V_g = -0.15$ V in the top panel of Fig. 6. Here, color again indicates the weight of the state in the SC; however, in contrast to Fig. 5, we do not just consider $k_x = 0$. We observe that hybridization with the superconductor may depend strongly on $k_x$, and in this case is generally strongest at large $k_x$.

### C. Superconducting properties at $B = 0$

We now turn our attention to the situation where the Al shell is in the superconducting state. The value of $W_{SC}$ at $k_F^{(n)}$ correlates well with the magnitude of the induced superconducting gap $\Delta_{\text{ind}}$ for a given subband. From the discussion of the previous subsection, we can then immediately conclude that different subbands will have different values of $\Delta_{\text{ind}}$. This is illustrated in the lower panel of Fig. 6, in which the subbands are shown for the case when $\Delta_0 \neq 0$, for energies of the order of $\Delta_0$. We see that bands with smaller $W_{SC}$ (shown as more blue) also have smaller $\Delta_{\text{ind}}$. The smallest value of $\Delta_{\text{ind}}$ is what fixes the superconducting gap for the SM-SC hybrid nanowire. This again emphasizes the importance of the strong confining potential to increase the hybridization between the two materials and thus a large induced gap.

Figure 7 (a) shows the evolution of the DOS with $V_g$. For $V_g < -0.6$ V all subbands in the SM hybridize very strongly with the Al subbands and, thus, have a large induced SC gap. As a result, there are no subgap states below $\varepsilon \approx 0.6\Delta_0$. As $V_g$ increases and the electrostatic potential becomes less confining, additional SM subbands become occupied for certain threshold values of $V_g$. As shown in Figure 7 (a), the number of subbands jumps at $V_g \approx (-0.6, -0.45, -0.15, -0.06, 0.03)$ V. In some cases the additional subbands have a smaller value of $W_{SC}$ resulting in a decrease of $\Delta_{\text{ind}}$. From Fig. 7 (b) we can see that this happens for the $V_g$ threshold values of -0.6 and -0.06 V. For $V_g > 0$, as shown in Fig. 5 (d), some of the subbands have states that are not localized close to

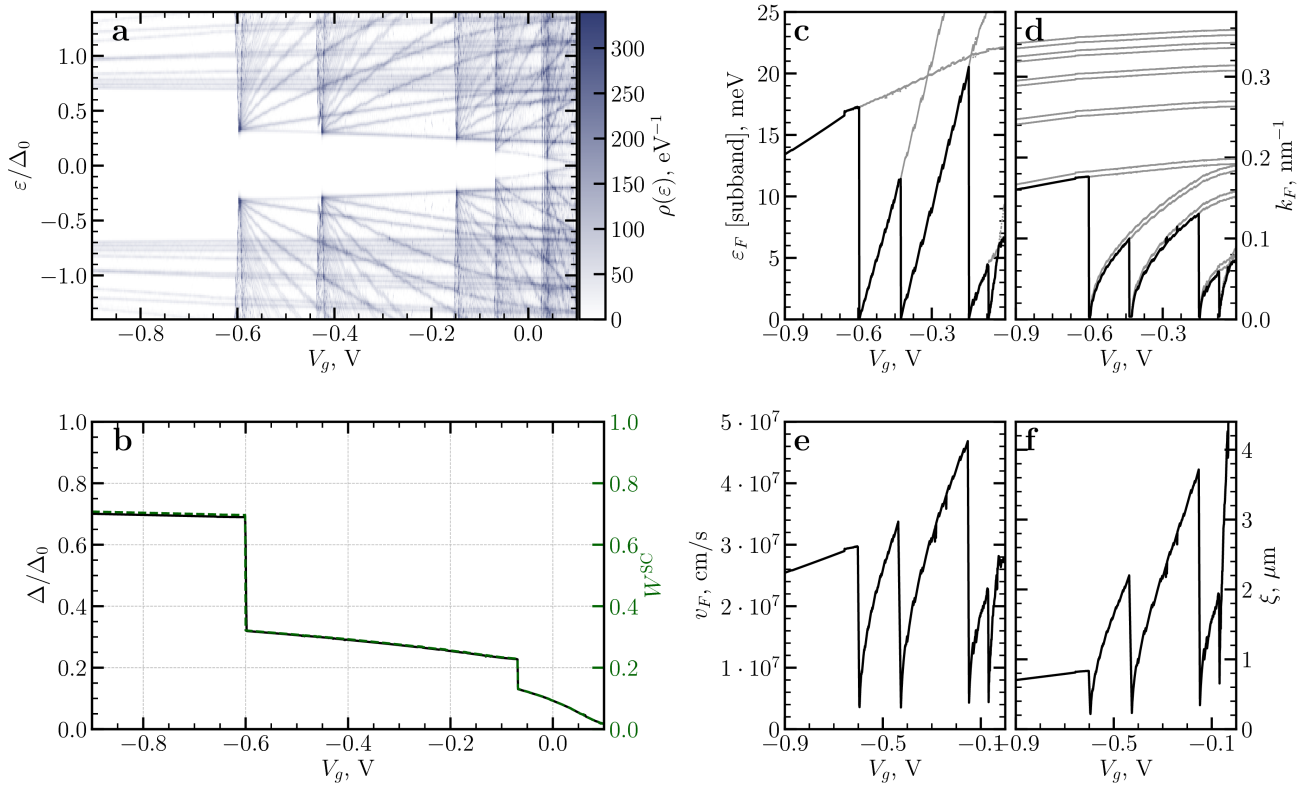


FIG. 7. Characterization of the superconducting state at $B = 0$, i.e. in the trivial $s$-wave superconducting phase, as a function of the gate voltage $V_g$: (a) Density of states, (b) induced gap (black) and weight in the superconductor (green), (c) Fermi energy, (d) Fermi momentum, (e) Fermi velocity and (f) SC coherence length. The discontinuities correspond to transitions where bands are driven below the chemical potential and thus become occupied (for an illustration, consider the transition between panels (a) and (c) of Fig. 8). In panel (b), the correspondence between the magnitude of the induced gap and the hybridization between SM and SC (as measured by the $W_{SC}$) is clearly shown. In panels (c) and (d), all bands are shown in grey, while the occupied band closest to the Fermi energy is highlighted in black.

the SM-SC interface and for which $W_{SC}$ is negligible. In this situation $\Delta_{\rm ind} \to 0$, and the system becomes gapless.

The evolution of $\Delta_{\rm ind}$ with $V_g$ is shown in Fig. 7 (b), together with the evolution of $W_{SC}$. From this figure we see that for $V_g < -0.6$ V, $\Delta_{\rm ind} \approx 0.75\Delta_0$. Furthermore, these results indicate that the evolution of the nanowire's superconducting gap with $V_g$ can be quite non-trivial and is closely related to $W_{SC}$. In order to have $\Delta_{\rm ind} \sim \Delta_0$, strong confining potentials ($V_g < -0.6$ V) are necessary. Conversely, in the case of a positive gate voltage, there are occupied states in the SM (see right panels of Fig. 5) which are far away from the SC and, as a result, are weakly proximitized.

Figures 7 (c)-(f) show the evolution of $\epsilon_F$, $k_F$, $v_F$, and $\xi$ with $V_g$ for the subband with the smallest induced superconducting gap, which determines $\Delta_{\rm ind}$ for the system. For a fixed number of subbands, as $V_g$ increases $\epsilon_F$, $k_F$ and $v_F$ grow, see Fig. 7 (c)-(e). Using the values of $v_F$, and $\Delta_{\rm ind}$ one can estimate the coherence length $\xi = v_F/\Delta_{\rm ind}$. From Fig. 7 (b) we see that change in $V_g$ preserving the number of occupied subbands leads to small changes in $\Delta_{\rm ind}$. Thus, the variations of $\xi$ are mostly due to the changes in $v_F$, see Fig. 7 (f). We see that, as long as the number of subbands is constant, $\xi$ grows with $V_g$ and follows $v_F$. The discontinuities in $\epsilon_F$, $k_F$, $v_F$, and $\xi$ appear when the number of occupied subbands changes, see Fig. 7 (a)-(f).

### D. Superconducting properties at finite magnetic fields

We now study how the properties of the SM-SC nanowire depend on the presence of the external magnetic field $B$ aligned along the longitudinal direction of the wire. As discussed in Sec. II, in our treatment the magnetic field enters only via the Zeeman term. For $B \sim 1$ T, orbital effect of the applied magnetic field is small since the SC is only 10 nm thick and in the regime of interest the wave functions in the SM are confined to the SM-SC interface within 20 nm range.

We start by investigating Zeeman splitting for the nanowire with multi-subband occupancy. The corresponding band structure is shown in Fig. 8 (a). Let's consider the gate voltage such that the highest occupied subband (shown in blue color) has small Fermi energy.

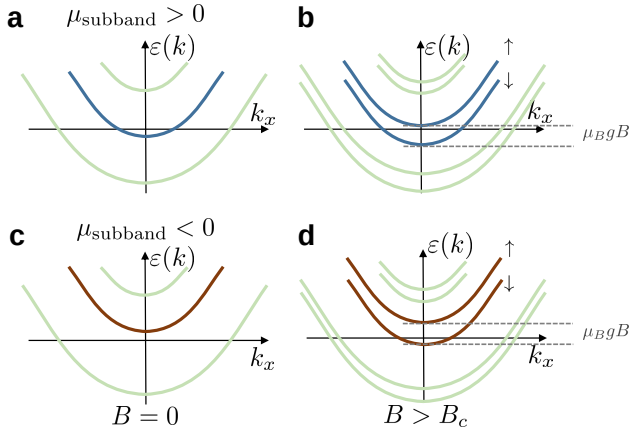


FIG. 8. Illustration of typical band structures, and the two different scenarios for the topological phase transition from an even to an odd number of occupied spin-subbands. The left two panels (a) and (c) show the situation without magnetic field, $B = 0$, where a subband is slightly below ((a), one spin-degenerate Fermi point) or above the chemical potential ((c), no Fermi points). Upon turning on a finite field that exceeds the distance from the bottom of these subbands to the chemical potential, the corresponding panel on the right is obtained, where an odd number of spin-split subbands is occupied.

The application of a magnetic field splits the subband and, at some critical field $B_c$, drives the minority subband across the Fermi level (provided $B_c$ is less than the critical field of the superconductor). This is illustrated in Fig. 8 (b). At this point, the majority subband becomes the highest occupied band, and, thus, many properties such as the Fermi energy, Fermi velocity and Fermi momentum change discontinuously.

Another scenario corresponds to Fig. 8 (c), where a band is just above the chemical potential. In this case, the gap of the system is determined by the lower occupied subband (shown in green). An increasing magnetic field splits the lowest *un*occupied band (shown in red) and eventually it becomes occupied.

In both these cases, we end up with an odd number of occupied subbands at large enough magnetic fields and, thus, the nanowire can be driven into the topological regime. However, the evolution of the gap with the magnetic field is drastically different in these two cases. This can seen in Fig. 9 which shows the evolution with magnetic field of the spectral gap $E_g$, effective Fermi energy for the highest occupied subband, and corresponding $k_F$, $v_F$, and $\xi$ for different gate voltages close to the the threshold value $V_{g,t} = -0.427$ V. This threshold value, corresponding to the gray curves in Fig. 9, corresponds to the gate voltage at which the relevant subband has exactly zero effective Fermi energy. As $B$ increases from zero the gap $E_g$ decreases and eventually vanishes at $B = B_c$ corresponding to the topological phase transition. For $B > B_c$, the nanowire is driven into the spinless regime with p-wave pairing potential. The p-wave gap

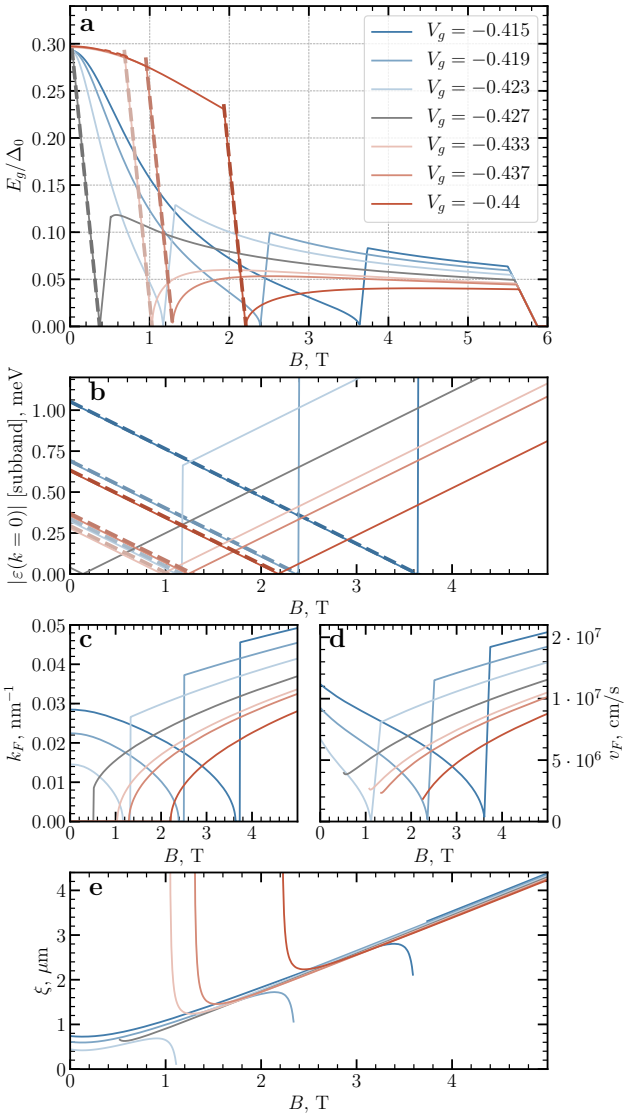


FIG. 9. The evolution of the system parameters as a function of a magnetic field $B$. Estimates for the (a) gap, (b) absolute value of the effective Fermi level of the subband $|\varepsilon(k_x = 0)|$ (where $k_x = 0$ is the location of the band bottom), (c) Fermi momentum, (d) Fermi velocity and (e) coherence length as a function of magnetic field. Colors correspond to different gate voltages: for blue lines, the gate voltage is more positive, leading to a situation as sketched in the upper two panels of Fig. 8. Red lines, on the other hand, have a more strongly negative gate voltage, thus leading to the situation of the two lower panels in Fig. 8. Gray color corresponds to the threshold value $V_g = -0.427$ V, at which the subband is characterized by a vanishing effective chemical potential.

exhibits a non-monotonic dependence on the magnetic field, and eventually vanishes because s-wave superconductor becomes normal. For our parameters this occurs at $B_{SC} = 5.8$ T. Note that we do not take into account orbital effects here so in practice $\Delta_0$ may vanish before that.

The blue family of curves in Fig. 9 (a) correspond to

the case when a highest-occupied subband has a small Fermi energy at zero field (top panels of Fig. 8). In that case, the gap at zero field is already set by the band that will eventually be split to give rise to topological superconductivity, and, thus, the gap evolves as a smooth function for $B < B_c$. At $B = B_c$ the minority subband crosses the Fermi level, and the topological gap is opened in the majority subband. As dicussed above, the properties of the Fermi points evolve discontinuously across the transition (panels b,c,d), and the gap increases rapidly into the topological phase (panel a).

At more negative gate voltages, the situation shown in Fig. 8 (c) and (d) is realized, corresponding to the red lines in Fig. 9. Here, the gap at $B = 0$ is determined by the next occupied subband. Upon the application of a magnetic field, the distance between the majority subband and the chemical potential eventually becomes smaller than the gap induced in the next-highest subband. This distance thus sets the spectral gap. The discontinuity of the gap function can be seen in Fig. 9 (a). At $B > B_c$ the topological gap is opened in the majority subband. In this cases, we plot in Fig. 9 the properties of the Fermi points only for the subbands that eventually become topological, and thus plot no values below the topological phase transition.

It is very interesting to notice that the size of the induced superconducting gap for $B = 0$ does not necessarily correlate with the size of the topological gap. This can be understood from the fact that the topological gap for $B > B_c$ is always opened in the same band, whereas the $\Delta_{\rm ind}$ at $B = 0$ is opened in a different band when $V_g$ becomes smaller than $V_g = -0.427$ V. As can be seen from Fig. 9 (c) the Fermi momentum $k_F$ for $B > B_c$, which corresponds always to the same band, increases with $V_g$. The topological gap increases with $k_F$ since the effective Rashba field is stronger at higher momentum, allowing the $s$-wave pairing to induce a larger gap. This is a very important result because $\Delta_{\rm ind}$ at $B \gtrsim B_c$ sets a crucial scale for the robustness of a topological qubit against error sources such as thermal fluctuations, diabatic corrections, disorder [99, 105, 106] etc.

### E. Effective g-factor

A crucial quantity to characterize the semiconductor-superconductor system is the effective g-factor of the hybrid system. Due to the drastically different g-factors in the two materials, this will depend intricately on the wave function hybridization between them. Furthermore, the g-factor is crucial in enabling a large and robust topological phase, since a large g-factor is necessary for the topological phase transition to occur at a magnetic field well below the critical value at which the Al shell is driven normal. A large effective $g$ is thus very helpful in achieving a sufficient separation between these scales.

The effective g-factor can be obtained from studying the Zeeman splitting of bands at $k_x = 0$, as illustrated in Fig. 8. In particular, since at $k_x = 0$ the spin-orbit terms in the Hamiltonian (4) vanish, the spin-splitting of the bands at $k_x = 0$ is entirely determined by the Zeeman term. As the change of the energy levels $\varepsilon(k_x = 0)$ is linear with the magnetic field, the absolute value of the g-factor can be extracted as $|g| = 2\frac{d\varepsilon(k=0)}{d\mu_B B}$. This linear fit for $B < B_c$ is illustrated in Fig. 9b with dashed lines. Note that when the gate voltage is such that the closest subband to the Fermi level is unoccupied (case (c) in Fig. 8), the slope near the gap-closing is the same as the one at $\varepsilon(k = 0)$, allowing for a reliable extraction of the g-factor from the tunneling conductance measurements [68]. This is shown in Fig. 9a by the dashed lines.

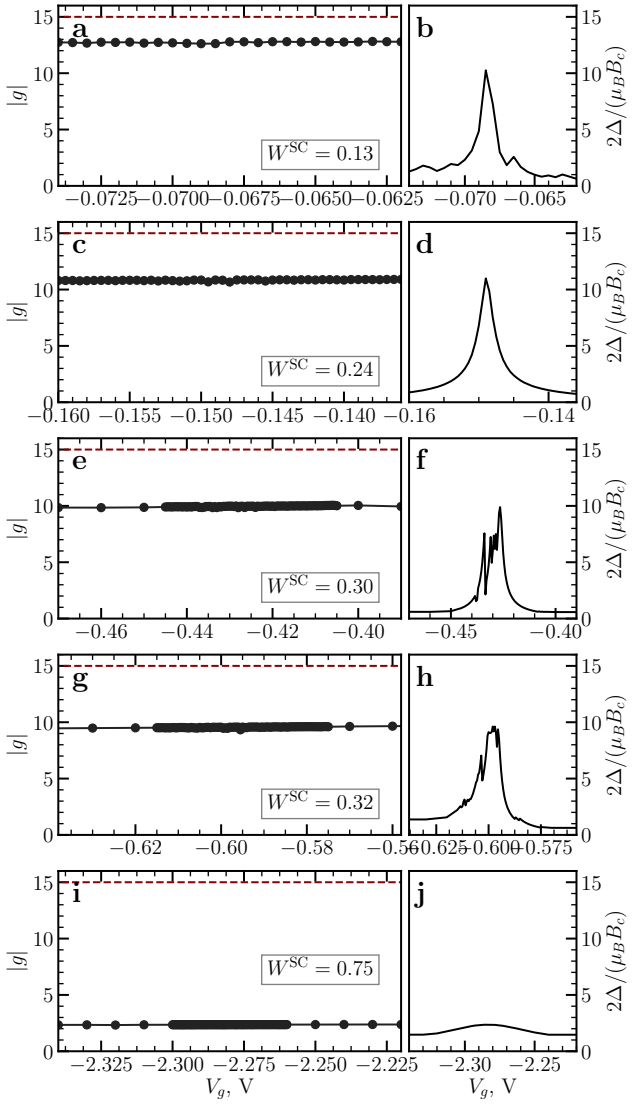


FIG. 10. Absolute value of g-factor (left column) and ratio of the induced gap to the critical magnetic field $2\Delta/(\mu_B B_c)$ (right column) as a function of gate voltage in the vicinity of threshold gate voltage values $V_g = -0.07$ (a,b), $-0.15$ (c,d), $-0.45$ (e,f), $-0.6$ (g,h), $-2.3$ (i,j) at which the number of subbands change in the system. The red dashed line is the absolute value of bare semiconductor g-factor $|g^{\rm bare}_{SM}|$.

In Fig. 10 we study the dependence of the extracted g-factor on the applied gate voltage in the vicinity of the threshold values at which the number of subbands change (see Fig. 7). As expected, we find every subband to be characterized by an almost constant g-factor, with significant changes occuring only at transitions between bands. When the hybridization between semi- and superconductor is weak, the g-factor is close to the bare semiconductor value $|g_{SM}^{\rm bare}| = 15$. Conversely, when the voltage is very negative (the value from Fig. 7 is written in every panel) and the hybridization between semi- and superconductor is strong the g-factor is almost as small as the bare superconducting g-factor $|g_{SM}^{\rm bare}| = 2$.

Additional information can be extracted from the ratio of the induced gap to the critical field, shown in the right column of Fig. 10. This quantity is easily accessible in experiments, and has been used in the experimental literature as a proxy for the g-factor [68]. Our results clearly show that unlike the g-factor, this quantity has a strong dependence on gate voltage over relatively small gate voltage variations. In particular, a resonant structure appears with a peak that corresponds to the gate voltage being tuned to the threshold value at which the subband crosses the effective chemical potential. Only at this point does this quantity reaches the values of the effective g-factor shown in the left column.

Figure 11 (a) shows the value of $g$ for different topological regions (see also the discussion in Sec. III F). We see that as $V_g$ becomes more negative the g-factor becomes smaller and approaches the value of $g$ in the SC. As stated above this is due to the fact that as $V_g$ becomes more negative the hybridization between SM and SC states becomes stronger as clearly shown by the evolution of $W_{SC}$, see Fig. 11 (b). Larger negative values of $V_g$ create an electrostatic potential that more strongly confines the SM states at the SM-SC interface. The tighter confinement results in a stronger hybridization between SM and SC states. Figure 11 (c) summarizes the important relation between strength of the hybridization between SM and SC states and the g-factor by showing the dependence of $|g|$ on $W_{SC}$. We see that qualitatively $g$ scales linearly with $W_{SC}$.

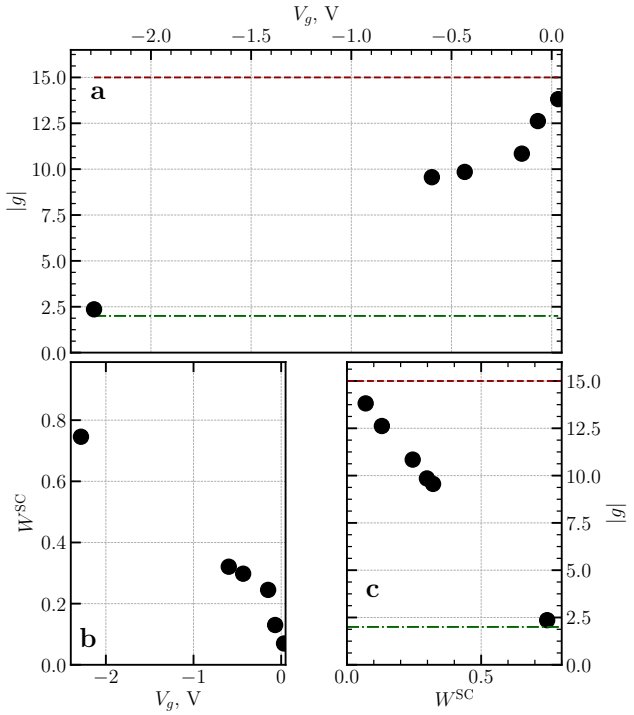


FIG. 11. Gate voltage dependence of (a) the absolute value of effective g-factor and (b) the weight in superconductor. Panel (c) relates $|g|$ to the weight in the superconductor $W_{SC}$. Dots represent typical values for the highest occupied band at a given gate voltage. The dashed horizontal values are the absolute values of the bare g-factor in the semiconductor (red) and superconductor (green). When the coupling to the superconductor is weak, as indicated by a small weight of the wavefunctions in the SC, the g-factor is close to the bare InAs value. The opposite limit occurs in the strongly hybridized regime at more negative gate voltages.

### F. Topological phase diagram

Figure 12 (a) shows the topological phase diagram in the $(V_g, B)$ plane. This is one of the most important result of this work: it relates the nature of the superconducting state of the quasi-1D hybrid nanowire to the experimentally relevant and tunable quantities – the gate voltage and the external magnetic field – rather than more abstract quantities such as the Fermi energy of the subbands and the Zeeman splitting, which are dependent on applied electric field. As discussed above, the relation between $V_g$ and the parameters characterizing the nanowire band structure, such as the subbands chemical potential and induced superconducting gap, is highly non-trivial given the nonlinear nature of the SP problem and the presence of multiple subbands. For this reason, for example, simplified models in which the subband chemical potential is assumed to be directly proportional to $V_g$ in general cannot be used to obtain a reliable phase diagram in the $(V_g, B)$ plane. Similarly, we have shown that for the g-factor we cannot take the bare value for the SM. One qualitative feature that emerges from the results shown in Fig. 12 (a) is how the shape and size of the topological regions depend on $V_g$. We see that for very large negative $V_g$ the critical magnetic field is higher than that for small negative values of $V_g$. This is due to the fact that the hybridization of the SM's and SC's states is stronger for larger negative $V_g$ and therefore the effective magnitude of $g$ is much smaller than $g_{SM}^{\rm bare}$ causing an increase of the critical field.

Fig. 12 (b) shows the dependence of the coherence length in the topological regime $\xi_t$, at the maximum of the topological gap for $B > B_c$, on the gate voltage. The coherence length shows a slight decrease with decreasing gate voltage, but it is much less pronounced than the value at $B = 0$ shown in Fig. 7 (f). The coherence

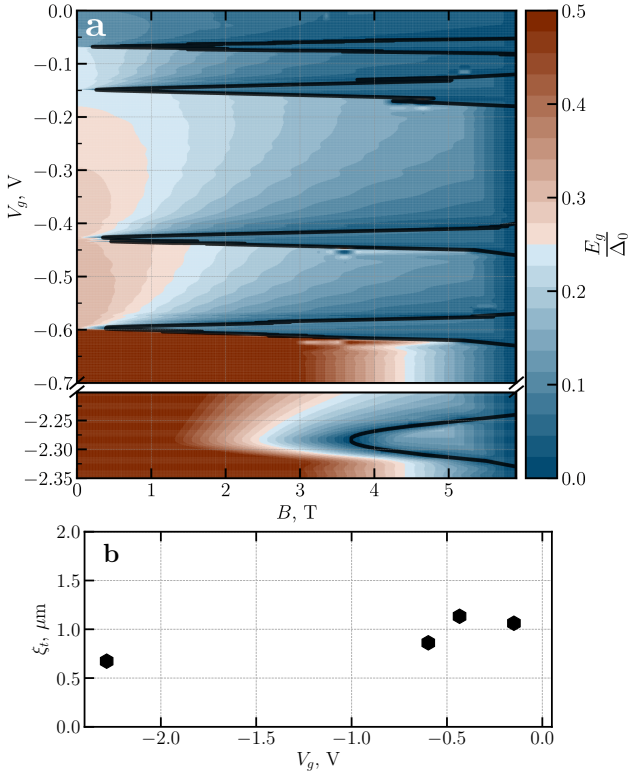


FIG. 12. (a) Topological phase diagram and magnitude of the spectral gap over a range of gate voltages from zero to very strongly negative. Clearly, the gap at zero field is largest for negative gate voltages where hybridization with the Al shell is strongest. The boundaries of the topological phase are marked with solid black lines. (b) Coherence length in the topological phase $\xi_t$ as a function of gate voltage.

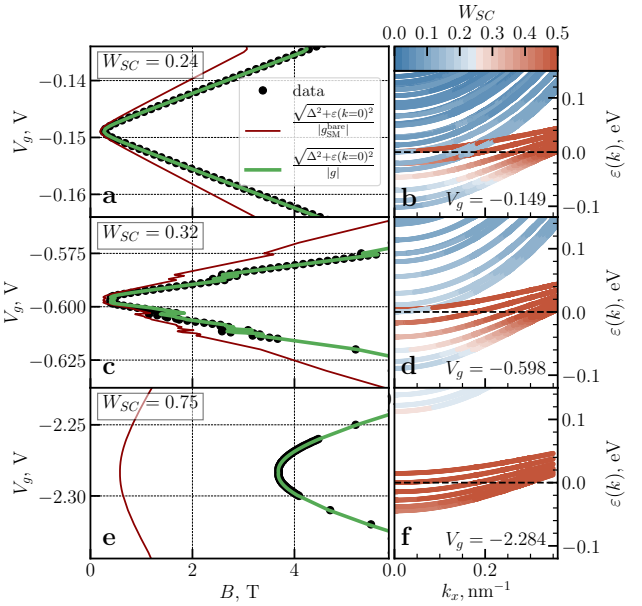


FIG. 13. Phase diagram, panels (a,c,e), and band structure, panels (b,d,f) in the vicinity of threshold gate voltages, corresponding to the change in the number of subbands: $V_g = -0.15$ (a,b); $V_g = -0.6$ (c,d); $V_g = -2.3$ (e,f). Black dots in the left panels correspond to the numerically calculated phase boundary. Red and green curves in left panels are the estimates obtained using the standard relation (9) and the bare SM's g-factor for the red curves and the renormalized g-factor Fig. 10, for the green ones.

length in the topological is a key quantity for designing topological qubits which rely on non-locality of MZMs.

We now compare the obtained phase diagram with the previous studies. In the case when the subband is occupied at $B = 0$ (the scenario shown in Figs. 8 (a)-(b)), the critical field $B_c$ can be expressed in terms of $\epsilon_F$ and $\Delta$ using the equation [27, 28]:

$$B_c = \frac{\sqrt{\epsilon_F^2 + \Delta^2}}{|g|}. \tag{8}$$

To also account for the scenario in which the subband undergoing the transition is unoccupied at $B = 0$, Figs. 8 (c)-(d), we can replace in Eq.(8) $\epsilon_F$ with $\epsilon(k = 0)$

$$B_c = \frac{\sqrt{[\epsilon(k = 0)]^2 + \Delta^2}}{|g|}. \tag{9}$$

Having obtained the dependence of $\epsilon(k = 0)$, $g$ and $\Delta$ on $V_g$, one can draw the boundaries in the $(V_g, B)$ plane of the topological phase diagram using Eq. (9). These boundaries are shown in green in the left panels of Fig. 13. We can see that they match exactly the boundaries obtained by identifying the value of $B$, $B_c$, where the gap is closing $\Delta_{\text{ind}} = 0$. We can see that Eq. (9), equivalent to Eq. (8) for the case when the subband is occupied, gives the correct boundaries *if* the renormalization of the g-factor is taken into account. On the other hand, if in Eq. (9) for $g$ we use the bare SM's g-factor Eq. (9) gives incorrect boundaries, shown in red in the left panels of Fig. 13. The boundaries obtained using the bare SM's g-factor overestimate the size of the topological region, especially when $V_g$ is strongly negative, see the bottom left panel of Fig. 13. As discussed above, this is due to the fact that the value of the g-factor, in the strong coupling regime, is strongly renormalized by the hybridization between the SM and SC states. The right panels in Fig. 13 show the band structure of the SM-SC nanowire close to the Fermi energy when $\Delta_0 \to 0$ for the appropriate values of $V_g$. We see that for very negative values of $V_g$, bottom panel, the SM states are very strongly hybridized with the SC states. This result is consistent with the fact that for this case $g$ is much smaller than $g_{SM}$ and therefore the topological region is much smaller that we would have obtained assuming $g = g_{SM}$.

## IV. SUMMARY AND CONCLUSIONS

We have studied properties of SM-SC nanowires in the presence of strong external electric fields. Our method is based on self-consistent Schrödinger-Poisson calculations which treat the semiconductor and the superconductor on equal footing. This approach allows one to take into account several semiconductor subbands which, we believe, are present in current experimental devices. We find that the treatment of the SM and SC at the same level is necessary to describe the strong-coupling regime characteristic to the high-quality epitaxial nanowires [56]. Such hybrid nanowires are very promising for the topological quantum computing applications as they exhibit large proximity-induced gaps and very low subgap conductance [55, 60, 64].

One of the most important results of our work is to provide an insight regarding the necessary conditions for achieving the strong-coupling regime in proximitized nanowires. We find that one of the key ingredients is the presence of an accumulation layer at the interface between the SM and the SC. The presence of an accumulation layer implies a strong confinement of the semiconductor wave function close to the SM-SC interface. Without such confinement, the significant mismatch between the Fermi velocities of SM and SC would significantly reduce the induced gap. This conclusion has recently been supported by angle-resolved photoemission spectroscopy experiments that have shown that in epitaxial InAs/Al systems the band offset $W$ is negative and therefore an electron accumulation layer is present.

We have investigated the effect of an external electric field which can be used to modify the confining potential and, thus, modify properties of electronic states in SM-SC devices. We find that external electric field can be used to change the number of subbands in the semiconductor, tunneling rate, induced gap, magnitude of the effective $g$ factor, coherence length $\xi$ etc. Our results show that the relation between $V_g$ and the quantities characterizing the electronic state of SM-SC quasi-1D nanowires is not trivial. The understanding of the interplay of $V_g$, number of subbands, and electronic properties is one of the most important results of our work.

Finally, we have obtained the topological phase diagram as a function of the gate voltage and magnetic field $B$. Previous works calculated the topological phase diagram in terms of phenomenological parameters such as effective chemical potential. Our work is the first to present a phase diagram in terms of $V_g$, the experimentally relevant and tunable quantity, instead of the chemical potential. We find that in the strong coupling regime the renormalization of the $g$ factor due to the strong hybridization between the SM's and the SC's states can significantly modify the topological phase diagram. For typical setups, the $g$ of the SC is smaller (in absolute value) than the SM's $g$ factor, and so the strong hybridization reduces the $g$ factor causing a decrease in the $(V_g, B)$ plane of the region where the system is in the topological phase.

Our work has important implications for current and future experiments aiming to realize Majorana-based topological qubits using SM-SC heterostructures as it allows one to optimize Majorana devices by tuning key parameters, $\Delta$, $g$, and $\xi$ with gates. Our results show that in the strong coupling the renormalization of $g$ can be quite significant increasing the minimal magnetic field necessary to drive the system into the topological phase. Thus, there is a sweet spot, and it is beneficial to operate in the intermediate coupling regime. This is critical information to design experiments aimed at realizing MZMs.

Finally, we discuss some limitations of our model. In this work, we do not take into account effect of disorder. There is a large body of papers investigating effect of the disorder in the semiconductor [31, 107–113] and at the interface [114] concluding that disorder leads to the subgap density of states (i.e. states below the induced gap). However, given the observation of a very small subgap density of states in recent experiments on high-quality proximitized nanowires [55, 60, 62, 64], we believe that the semiconductor, as well as SC-SM interface, are quite clean. The situation with Al is less clear since the presence of the native oxide covering Al may lead to significant impurity scattering. The effect of the disorder in the superconductor is two-fold - a) it may relax the constraint on momentum conservation and may lead to the enhancement of the induced SC gap as well as the suppression of the SC coherence length; impurity scattering should also smear out sharp features in the induced gap as well as other physical observables; b) impurities in the SC may induce subgap states [115–118]. Once again the optimization of the tunneling rate between SM-SC is very important [115, 118]. Understanding the effects of the disorder in realistic proximitized nanowires is an interesting open problem. Another limitation of our model is the lack of orbital effects due to the magnetic field. Due to the strong geometry dependence of the orbital effect [93], however, a careful treatment of it needs to go beyond the slab model discussed here.

Finally, we emphasize that, although in this work we focused on InAs/Al hybrid nanowires, the Schrödinger-Poisson approached proposed in this work can be used to study other heterostructures such as InSb/Al nanowires, two-dimensional SM-SC heterostructure and the quasi 1D channels created by electrostatic confinement in such structures.

## V. ACKNOWLEDGMENTS

We are grateful to Karsten Flensberg, Michael Wimmer, Adriaan Vuik, Bas Nijholt, Jan Gukelberger, John Gamble, Hao Zhang, Mingtang Deng and Saulius Vaitiekénas for stimulating discussions. ER acknowledges support from NSF-DMR-1455233, ONR-N00014-16-1-3158, and ARO-W911NF-16-1-0387.

[1] C. W. J. Beenakker, Annu. Rev. Condens. Matter Phys. **4**, 113 (2013), arXiv:1112.1950.
[2] J. Alicea, Reports on Progress in Physics **75**, 076501 (2012), arXiv:1202.1293.
[3] M. Leijnse and K. Flensberg, Semiconductor Science Technology **27**, 124003 (2012), arXiv:1206.1736.
[4] T. D. Stanescu and S. Tewari, J. Phys. Condens. Matter **25**, 233201 (2013), arXiv:1302.5433.
[5] S. R. Elliott and M. Franz, Rev. Mod. Phys. **87**, 137 (2015).
[6] S. Das Sarma, M. Freedman, and C. Nayak, npj Quantum Inf. **1** (2015).
[7] M. Sato and S. Fujimoto, J. Phys. Soc. Japan **85**, 72001 (2016).
[8] R. Aguado, ArXiv e-prints (2017), arXiv:1711.00011 [cond-mat.supr-con].
[9] R. M. Lutchyn, E. P. A. M. Bakkers, L. P. Kouwenhoven, P. Krogstrup, C. M. Marcus, and Y. Oreg, ArXiv e-prints (2017), arXiv:1707.04899 [cond-mat.supr-con].
[10] N. Read and D. Green, PRB **61**, 10267 (2000).
[11] D. A. Ivanov, Phys. Rev. Lett. **86**, 268 (2001).
[12] A. Kitaev, Phys. Uspekhi **44**, 131 (2001).
[13] G. Moore and N. Read, Nucl. Phys. B **360**, 362 (1991).
[14] P. Bonderson, M. Freedman, and C. Nayak, Phys. Rev. Lett. **101**, 10501 (2008).
[15] F. Wilczek, Nature Phys. **5**, 614 (2009).
[16] A. Stern, Nature (London) **464**, 187 (2010).
[17] P. W. Brouwer, Science **336**, 989 (2012).
[18] P. A. Lee, Science (80-. ). **346**, 545 (2014).
[19] A. Y. Kitaev, Ann. Phys. (N. Y). **303**, 2 (2003).
[20] C. Nayak, S. Simon, A. Stern, M. Freedman, and S. Das Sarma, Rev. Mod. Phys. **80**, 1083 (2008), arXiv:0707.1889.
[21] L. Fu and C. L. Kane, Phys. Rev. Lett. **100**, 096407 (2008).
[22] L. Fu and C. L. Kane, Phys. Rev. B **79**, 161408(R) (2009).
[23] A. Cook and M. Franz, Phys. Rev. B **84**, 201105 (2011).
[24] H.-H. Sun *et al.*, Phys. Rev. Lett. **116**, 257003 (2016).
[25] J. D. Sau, R. M. Lutchyn, S. Tewari, and S. D. Sarma, Phys. Rev. Lett. **104**, 040502 (2010).
[26] J. Alicea, Phys. Rev. B **81**, 125318 (2010).
[27] R. Lutchyn, J. Sau, and S. Das Sarma, Phys. Rev. Lett. **105**, 077001 (2010), arXiv:1002.4033.
[28] Y. Oreg, G. Refael, and F. von Oppen, Phys. Rev. Lett. **105**, 177002 (2010), arXiv:1003.1145.
[29] S. B. Chung, H.-J. Zhang, X.-L. Qi, and S.-C. Zhang, Phys. Rev. B **84**, 060510 (2011).
[30] M. Duckheim and P. W. Brouwer, Phys. Rev. B **83**, 054513 (2011).
[31] A. C. Potter and P. A. Lee, Phys. Rev. B **85**, 094516 (2012).
[32] T.-P. Choy, J. M. Edge, A. R. Akhmerov, and C. W. J. Beenakker, Phys. Rev. B **84**, 195442 (2011).
[33] I. Martin and A. F. Morpurgo, Phys. Rev. B **85**, 144505 (2012).
[34] S. Nadj-Perge, I. K. Drozdov, B. A. Bernevig, and A. Yazdani, Phys. Rev. B **88**, 020407 (2013).
[35] J. Klinovaja, P. Stano, A. Yazdani, and D. Loss, Physical Review Letters **111**, 186805 (2013), arXiv:1307.1442 [cond-mat.mes-hall].
[36] B. Braunecker and P. Simon, Physical Review Letters **111**, 147202 (2013), arXiv:1307.2431 [cond-mat.mes-hall].
[37] M. M. Vazifeh and M. Franz, Physical Review Letters **111**, 206802 (2013), arXiv:1307.2279 [cond-mat.mes-hall].
[38] F. Pientka, L. I. Glazman, and F. von Oppen, Phys. Rev. B **88**, 155420 (2013).
[39] S. Nakosai, Y. Tanaka, and N. Nagaosa, Phys. Rev. B **88**, 180503 (2013).
[40] Y. Kim, M. Cheng, B. Bauer, R. M. Lutchyn, and S. Das Sarma, Phys. Rev. B **90**, 60401 (2014).
[41] P. M. R. Brydon, S. Das Sarma, H.-Y. Hui, and J. D. Sau, Phys. Rev. B **91**, 064505 (2015), arXiv:1407.6345 [cond-mat.mes-hall].
[42] J. Li, H. Chen, I. K. Drozdov, A. Yazdani, B. A. Bernevig, and A. H. MacDonald, Phys. Rev. B **90**, 235433 (2014).
[43] A. Heimes, P. Kotetes, and G. Schön, Phys. Rev. B **90**, 60507 (2014).
[44] J. Röntynen and T. Ojanen, Phys. Rev. Lett. **114**, 236803 (2015).
[45] S. Nadj-Perge, I. K. Drozdov, J. Li, H. Chen, S. Jeon, J. Seo, A. H. MacDonald, B. A. Bernevig, and A. Yazdani, Science (2014), 10.1126/science.1259327.
[46] M. Ruby, F. Pientka, Y. Peng, F. von Oppen, B. W. Heinrich, and K. J. Franke, Phys. Rev. Lett. **115**, 197204 (2015).
[47] R. Pawlak, M. Kisiel, J. Klinovaja, T. Meier, S. Kawai, T. Glatzel, D. Loss, and E. Meyer, npj Quantum Mechanics **2**, 16035 (2016), arXiv:1505.06078 [physics.atm-clus].
[48] J. Zhang, Y. Kim, E. Rossi, and R. M. Lutchyn, Phys. Rev. B **93**, 024507 (2016).
[49] V. Mourik, K. Zuo, S. M. Frolov, S. R. Plissard, E. P. A. M. Bakkers, and L. P. Kouwenhoven, Science **336**, 1003 (2012), arXiv:1204.2792.
[50] L. P. Rokhinson, X. Liu, and J. K. Furdyna, Nat. Phys. **8**, 795 (2012).
[51] M. T. Deng, C. L. Yu, G. Y. Huang, M. Larsson, P. Caroff, and H. Q. Xu, Nano Lett. **12**, 6414 (2012).
[52] H. O. H. Churchill, V. Fatemi, K. Grove-Rasmussen, M. T. Deng, P. Caroff, H. Q. Xu, and C. M. Marcus, Phys. Rev. B **87**, 241401 (2013), arXiv:1303.2407.
[53] A. Das, Y. Ronen, Y. Most, Y. Oreg, M. Heiblum, and H. Shtrikman, Nat. Phys. **8**, 887 (2012).
[54] A. D. K. Finck, D. J. Van Harlingen, P. K. Mohseni, K. Jung, and X. Li, Phys. Rev. Lett. **110**, 126406 (2013).
[55] W. Chang, S. Albrecht, T. Jespersen, F. Kuemmeth, P. Krogstrup, J. Nygård, and C. Marcus, Nat. Nanotechnol. **10**, 232 (2015), arXiv:1411.6255.
[56] P. Krogstrup, N. L. B. Ziino, W. Chang, S. M. Albrecht, M. H. Madsen, E. Johnson, J. Nygård, C. M. Marcus, and T. S. Jespersen, Nat. Mater. **14**, 400 (2015).
[57] S. M. Albrecht, A. P. Higginbotham, M. Madsen, F. Kuemmeth, T. S. Jespersen, J. Nygård, P. Krogstrup, and C. M. Marcus, Nature (London) **531**, 206 (2016), arXiv:1603.03217.
[58] H. Zhang, Ö. Gül, S. Conesa-Boj, K. Zuo, V. Mourik, F. K. de Vries, J. van Veen, D. J. van Woerkom, M. P.

Nowak, M. Wimmer, D. Car, S. Plissard, E. P. A. M. Bakkers, M. Quintero-Pérez, S. Goswami, K. Watanabe, T. Taniguchi, and L. P. Kouwenhoven, "Ballistic Majorana nanowire devices," (2016), arXiv:1603.04069.
[59] J. Chen, P. Yu, J. Stenger, M. Hocevar, D. Car, S. Plissard, E. Bakkers, T. Stanescu, and S. Frolov, ArXiv e-prints (2016), arXiv:1610.04555 [cond-mat.mes-hall].
[60] M. Deng, S. Vaitiekénas, E. Hansen, J. Danon, M. Leijnse, K. Flensberg, J. Nygård, P. Krogstrup, and C. Marcus, Science **354**, 1557 (2016).
[61] H. J. Suominen, M. Kjaergaard, A. R. Hamilton, J. Shabani, C. J. Palmstrøm, C. M. Marcus, and F. Nichele, ArXiv e-prints (2017), arXiv:1703.03699 [cond-mat.mes-hall].
[62] F. Nichele, A. C. C. Drachmann, A. M. Whiticar, E. C. T. O'Farrell, H. J. Suominen, A. Fornieri, T. Wang, G. C. Gardner, C. Thomas, A. T. Hatke, P. Krogstrup, M. J. Manfra, K. Flensberg, and C. M. Marcus, Physical Review Letters **119**, 136803 (2017), arXiv:1706.07033 [cond-mat.mes-hall].
[63] S. Gazibegovic, D. Car, H. Zhang, S. Balk, J. Logan, M. de Moor, M. Cassidy, R. Schmits, D. Xu, G. Wang, P. Krogstrup, R. het Veld, J. Shen, D. Bouman, B. Shojaei, D. Pennachio, J. Lee, P. van Veldhoven, S. Koelling, M. Verheijen, L. Kouwenhoven, C. Palmstrøm, and E. Bakkers, ArXiv e-prints (2017), arXiv:1705.01480 [cond-mat.mes-hall].
[64] H. Zhang, C.-X. Liu, S. Gazibegovic, D. Xu, J. A. Logan, G. Wang, N. van Loo, J. D. S. Bommer, M. W. A. de Moor, D. Car, R. L. M. O. het Veld, P. J. van Veldhoven, S. Koelling, M. A. Verheijen, M. Pendharkar, D. J. Pennachio, B. Shojaei, J. S. Lee, C. J. Palmstrom, E. P. A. M. Bakkers, S. Das Sarma, and L. P. Kouwenhoven, ArXiv e-prints (2017), arXiv:1710.10701 [cond-mat.mes-hall].
[65] H. Zhang, Ö. Gül, S. Conesa-Boj, M. Nowak, M. Wimmer, K. Zuo, V. Mourik, F. K. de Vries, J. van Veen, M. W. A. de Moor, J. D. S. Bommer, D. van Woerkom, D. Car, S. Plissard, E. P.A.M. Bakkers, M. Quintero-Pérez, M. C. Cassidy, S. Koelling, S. Goswami, and L. P. Kouwenhoven, *Nature Communications*, **8**, 16025 (2017).
[66] J. E. Sestoft, T. Kanne, A. Nørskov Gejl, M. von Soosten, J. S. Yodh, D. Sherman, B. Tarasinski, M. Wimmer, E. Johnson, M. Deng, J. Nygård, T. Sand Jespersen, C. M. Marcus, and P. Krogstrup, ArXiv e-prints (2017), arXiv:1711.06864 [cond-mat.mes-hall].
[67] M. T. Deng, S. Vaitiek´énas, E. Prada, P. San-Jose, J. Nygård, P. Krogstrup, R. Aguado, and C. M. Marcus, ArXiv e-prints (2017), arXiv:1712.03536 [cond-mat.mes-hall].
[68] S. Vaitiekénas, M. Deng, J. Nygård, P. Krogstrup, and C. Marcus, ArXiv e-prints (2017), arXiv:1710.04300 [cond-mat.mes-hall].
[69] D. Laroche, D. Bouman, D. J. van Woerkom, A. Proutski, C. Murthy, D. I. Pikulin, C. Nayak, R. J. J. van Gulik, J. Nygård, P. Krogstrup, L. P. Kouwenhoven, and A. Geresdi, ArXiv e-prints (2017), arXiv:1712.08459 [cond-mat.mes-hall].
[70] P. Krogstrup, N. L. B. Ziino, W. Chang, S. M. Albrecht, M. H. Madsen, E. Johnson, J. Nygård, C. M. Marcus, and T. S. Jespersen, Nature Mater. **14**, 400 (2015), arXiv:1411.6254.
[71] R. T. Tung, Materials Science & Engineering R-reports **35**, 1 (2001).
[72] H. Lüth, *Solid Surfaces, Interfaces and Thin Films*, Graduate Texts in Physics (Springer Berlin Heidelberg, 2011).
[73] S. Abe, T. Inaoka, and M. Hasegawa, Phys. Rev. B **66**, 205309 (2002).
[74] B. Y. Feng, S. Y. Huang, J. Y. Wang, D. Pan, J. H. Zhao, and H. Q. Xu, J. Appl. Phys. **119**, 054304 (2016).
[75] S. Schuwalow and P. Krogstrup et al., To be published.
[76] L. A. Landau, S. Plugge, E. Sela, A. Altland, S. M. Albrecht, and R. Egger, Phys. Rev. Lett. **116**, 50501 (2016).
[77] S. Vijay and L. Fu, Phys. Scr. Vol. T **168**, 14002 (2016), arXiv:1509.08134 [cond-mat.mes-hall].
[78] S. Plugge, L. A. Landau, E. Sela, A. Altland, K. Flensberg, and R. Egger, Phys. Rev. B **94**, 174514 (2016).
[79] T. Karzig, C. Knapp, R. M. Lutchyn, P. Bonderson, M. B. Hastings, C. Nayak, J. Alicea, K. Flensberg, S. Plugge, Y. Oreg, C. M. Marcus, and M. H. Freedman, Phys. Rev. B **95**, 235305 (2017).
[80] S. Plugge, A. Rasmussen, R. Egger, and K. Flensberg, New J. Phys. **19**, 12001 (2017), arXiv:1609.01697.
[81] F. Stern, Phys. Rev. B **5**, 4891 (1972).
[82] T. Ando, A. B. Fowler, and F. Stern, Rev. Mod. Phys. **54**, 437 (1982).
[83] F. Stern and S. Dassarma, Phys. Rev. B **30**, 840 (1984).
[84] T. D. Stanescu, R. M. Lutchyn, and S. Das Sarma, Phys. Rev. B **84**, 144522 (2011), arXiv:1106.3078.
[85] E. Prada, P. San-Jose, and R. Aguado, Phys. Rev. B **86**, 180503 (2012), arXiv:1203.4488 [cond-mat.mes-hall].
[86] D. Rainis, L. Trifunovic, J. Klinovaja, and D. Loss, Phys. Rev. B **87**, 24515 (2013).
[87] W. S. Cole, S. Das Sarma, and T. D. Stanescu, Phys. Rev. B **92**, 174511 (2015).
[88] C. Reeg, D. Loss, and J. Klinovaja, Phys. Rev. B **96**, 125426 (2017).
[89] D. Sticlet, B. Nijholt, and A. Akhmerov, Phys. Rev. B **95**, 115421 (2017).
[90] A. A. Soluyanov, D. Gresch, M. Troyer, R. M. Lutchyn, B. Bauer, and C. Nayak, Phys. Rev. B **93**, 115317 (2016), arXiv:1510.02025 [cond-mat.mtrl-sci].
[91] A. Vuik, D. Eeltink, A. R. Akhmerov, and M. Wimmer, New J. Phys. **18**, 33013 (2016).
[92] V. E. Degtyarev, S. V. Khazanova, and N. V. Demarina, Scientific Reports **7**, 3411 (2017).
[93] G. W. Winkler, D. Varjas, R. Skolasinski, A. A. Soluyanov, M. Troyer, and M. Wimmer, Phys. Rev. Lett. **119**, 037701 (2017).
[94] I. Vurgaftman, J. R. Meyer, and L. R. Ram-Mohan, Journal of Applied Physics **89**, 5815 (2001).
[95] C. R. Pidgeon, D. L. Mitchell, and R. N. Brown, Phys. Rev. **154**, 737 (1967).
[96] I. van Weperen, B. Tarasinski, D. Eeltink, V. S. Pribiag, S. R. Plissard, E. P. A. M. Bakkers, L. P. Kouwenhoven, and M. Wimmer, Phys. Rev. B **91**, 201413 (2015).
[97] J. F. Cochran and D. E. Mapother, Phys. Rev. **111**, 132 (1958).
[98] I. Tan, G. L. Snider, L. D. Chang, and E. L. Hu, J. Appl. Phys. **68**, 4071 (1990).
[99] C. Knapp, T. Karzig, R. Lutchyn, and C. Nayak, ArXiv e-prints (2017), arXiv:1711.03968 [cond-mat.mes-hall].
[100] Note that the presence of $z$-dependent masses, spin-orbit coupling and potentials does not allow to separate

variables in $z$ and other directions and therefore a diagonalization of a Hamiltonian matrix would be required for every different set of momenta.
[101] D. G. Anderson, J. ACM **12**, 547 (1965).
[102] R. M. Lutchyn, T. D. Stanescu, and S. Das Sarma, Phys. Rev. Lett. **106**, 127001 (2011).
[103] C. W. Groth, M. Wimmer, A. R. Akhmerov, and X. Waintal, New Journal of Physics **16**, 063065 (2014).
[104] Other 1D subbands in Al having effective Fermi energies larger than 0.25 eV are not shown since they do not hybridize with the semiconductor subbands due to energy-momentum conservation. However, when Al is disordered, these subbands may hybridize and, therefore, have to be taken into account.
[105] M. Cheng, R. M. Lutchyn, and S. Das Sarma, Phys. Rev. B **85**, 165124 (2012), arXiv:1112.3662 [cond-mat.supr-con].
[106] C.-X. Liu, J. Sau, and S. Das Sarma, Phys. Rev. B **95**, 54502 (2017), arXiv:1610.08042 [cond-mat.mes-hall].
[107] O. Motrunich, K. Damle, and D. A. Huse, Phys. Rev. B **63**, 224204 (2001).
[108] P. W. Brouwer, M. Duckheim, A. Romito, and F. von Oppen, Phys. Rev. B **84**, 144526 (2011).
[109] T. D. Stanescu, R. M. Lutchyn, and S. Das Sarma, Phys. Rev. B **84**, 144522 (2011), arXiv:1106.3078.
[110] A. R. Akhmerov, J. P. Dahlhaus, F. Hassler, M. Wimmer, and C. W. J. Beenakker, Phys. Rev. Lett. **106**, 57001 (2011).
[111] A. M. Lobos, R. M. Lutchyn, and S. Das Sarma, Phys. Rev. Lett. **109**, 146403 (2012).
[112] İ. Adagideli, M. Wimmer, and A. Teker, Phys. Rev. B **89**, 144506 (2014).
[113] S. S. Hegde and S. Vishveshwara, Phys. Rev. B **94**, 115166 (2016).
[114] S. Takei, B. M. Fregoso, H.-Y. Hui, A. M. Lobos, and S. Das Sarma, Phys. Rev. Lett. **110**, 186803 (2013).
[115] R. M. Lutchyn, T. D. Stanescu, and S. Das Sarma, Phys. Rev. B **85**, 140513 (2012).
[116] H.-Y. Hui, J. D. Sau, and S. Das Sarma, Phys. Rev. B **92**, 174512 (2015).
[117] W. S. Cole, J. D. Sau, and S. Das Sarma, Phys. Rev. B **94**, 140505 (2016).
[118] D. E. Liu, E. Rossi, and R. M. Lutchyn, ArXiv e-prints (2017), arXiv:1711.04056 [cond-mat.mes-hall].